Investigation of the nonlinear refractive index of single-crystalline thin gold films and plasmonic nanostructures

Sebastian Goetz[1] · Gary Razinskas[2] · Enno Krauss[2] · Christian Dreher[1] ·
Matthias Wurdack[1] · Peter Geisler[2] · Monika Pawłowska[1,3] · Bert Hecht[2,4] ·
Tobias Brixner[1,4]

Abstract The nonlinear refractive index of plasmonic materials may be used to obtain nonlinear functionality, e.g., power-dependent switching. Here, we investigate the nonlinear refractive index of single-crystalline gold in thin layers and nanostructures on dielectric substrates. In a first step, we implement a z-scan setup to investigate ~100-μm-sized thin-film samples. We determine the nonlinear refractive index of fused silica, $n_2(SiO_2) = 2.9 \times 10^{-20}$ m^2/W, in agreement with literature values. Subsequent z-scan measurements of single-crystalline gold films reveal a damage threshold of 0.22 TW/cm^2 and approximate upper limits of the real and imaginary parts of the nonlinear refractive index, $|n_2'(Au)| < 1.2 \times 10^{-16}$ m^2/W and $|n_2''(Au)| < 0.6 \times 10^{-16}$ m^2/W, respectively. To further determine possible effects of a nonlinear refractive index in plasmonic circuitry, interferometry is proposed as a phase-sensitive probe. In corresponding nanostructures, relative phase changes between two propagating near-field modes are converted to amplitude changes by mode interference. Power-dependent experiments using sub-10-fs near-infrared pulses and diffraction-limited resolution (NA = 1.4) reveal linear behavior up to the damage threshold (0.23 times relative to that of a solid single-crystalline gold film). An upper limit for the nonlinear power-dependent phase change between two propagating near-field modes is determined to $\Delta\varphi < 0.07$ rad.

✉ Bert Hecht
hecht@physik.uni-wuerzburg.de

✉ Tobias Brixner
brixner@phys-chemie.uni-wuerzburg.de

1 Institut für Physikalische und Theoretische Chemie, Universität Würzburg, Am Hubland, 97074 Würzburg, Germany

2 Nano-Optics and Biophotonics Group, Experimentelle Physik 5, Universität Würzburg, Am Hubland, 97074 Würzburg, Germany

3 Present Address: Nencki Institute for Experimental Biology, Polish Academy of Sciences, 3 Pasteur Street, 02-093 Warsaw, Poland

4 Röntgen Research Center for Complex Material Systems (RCCM), Universität Würzburg, Am Hubland, 97074 Würzburg, Germany

1 Introduction

The use of highly confined near-field excitations holds promise to create unique integrated device designs. Plasmonic circuits can outperform photonic devices in terms of integration density and electronic circuits in terms of transmission bandwidth [1–3]. Far-field radiation can be effectively coupled into and out of such plasmonic circuits with the help of optical antennas [4, 5]. Crucial for the design of logical elements in plasmonic circuitry is the ability to influence the near-field propagation direction. In devices realized so far, directional switching relies on linear interference of multiple plasmonic modes [6–8]. However, true conditional switching action as occurring in electric transistors requires the utilization of nonlinear effects. One way to realize nonlinearities in plasmonic nanocircuitry consists in the combination of plasmonic materials with dielectrics having large higher-order susceptibilities. For example, the use of chalcogenide glasses has been proposed [9, 10]. However, the high precision required to embed such materials into plasmonic nanostructures constitutes a major

obstacle for their realization. An alternative approach consists in directly using the nonlinear Kerr-type response of the electron plasma in metals [11], which has been demonstrated for example by four-wave mixing at gold surfaces supporting surface plasmons [12, 13] and in experiments showing third-harmonic generation in single plasmonic nanoparticles [14] and optical nanoantennas [15, 16]. The latter type of experiments make use of the fact that the inherent optical nonlinearity of plasmonic materials can be enhanced in well-designed, high-quality nanostructures in which considerable near-field intensity enhancement can be achieved.

The design of plasmonic circuitry in which effects of the third-order nonlinearity of gold can be observed suffers from the lack of reliable knowledge of the nonlinear optical constants in the relevant spectral range. Uncertainties are related to the dependence of the nonlinear response on the crystalline structure as data obtained so far were recorded for multi-crystalline thin films [17–21] and data for single-crystalline gold films do not exist. Furthermore, it is unclear what effect the nonlinear refractive index has on propagation phenomena in plasmonic circuits.

Here, we present measurements of the nonlinear refractive index of a homogeneous single-crystalline gold layer. In a second step, we introduce a new method to reveal nonlinear effects in plasmonic circuitry fabricated from single-crystalline gold. The nonlinear refractive index is studied using a z-scan experiment. To investigate the effects of third-order nonlinearity in plasmonic nanocircuitry, we designed phase-sensitive nanointerferometers that allow us to retrieve upper bounds for nonlinear effects in plasmon propagation and in the formation of mode superpositions. Our results offer some insight into the feasibility of nonlinear all-plasmonic switching based on gold.

2 Implementation of the z-scan method

The beam distortion resulting from the phenomenon of self-focusing of a high-power Gaussian beam within a nonlinear medium can be experimentally utilized to extract the medium's complex nonlinear refractive index $n_2 = n_2' + i \cdot n_2''$, with real part n_2' and imaginary part n_2''. For this purpose, Sheik-Bahae et al. [22, 23] developed a sensitive measurement technique, the so-called z-scan method. Essentially, the sample under investigation is scanned along the longitudinal (z) direction through the focus of a laser beam, while simultaneously the fraction of light transmitted by a small, well-defined aperture placed in the diverging beam after the sample is detected in the far field (closed-aperture z-scan). This far-field transmittance shows a characteristic dependency on the exact sample position with respect to

the focus caused by the self-focusing effect and allows the derivation of the sample material's n_2.

The shape of the z-scan transmittance curve is distorted by nonlinear absorption effects, e.g., due to two-photon absorption or saturable absorption. However, the nonlinear absorption can be measured separately by recording the whole transmittance with the aperture removed (open-aperture z-scan) allowing the determination of the imaginary part of the refractive index n_2''. At the same time, an estimate for the real part of the nonlinear refractive index n_2' for samples showing nonlinear absorption can be obtained by a procedure that involves performing both an open-aperture and a closed-aperture z-scan and a subsequent division of the latter by the former [23].

In such a normalized z-scan, the peak-to-valley transmittance change ΔT_{p-v} (i.e., the vertical distance between maximum and minimum transmittance) is related to n_2' using well-known equations of z-scan theory [24]. The real part of the nonlinear refractive index can be determined as follows

$$n_2' = \frac{1.232 \, \lambda \, \tau \, w_0^2}{(1 - S)^{0.25} E \, L_{\text{eff}}} \Delta T_{\text{p-v}}, \tag{1}$$

where λ is the vacuum wavelength, τ is the pulse length, w_0 is the beam waist radius, S is the aperture transmittance in absence of the sample, and E is the pulse energy. The effective length of the sample L_{eff} is defined as follows

$$L_{\text{eff}} = \frac{1 - \exp(-\alpha L)}{\alpha} \tag{2}$$

with the linear absorption coefficient α and the physical length of the sample L. In this context, L_{eff} is referring to the intensity decay.

From the open-aperture z-scan, the imaginary part of the nonlinear refractive index can be estimated by [23]

$$n_2'' = -\frac{\lambda \, \tau \, w_0^2}{\sqrt{2} \, E \, L_{eff}} \Delta T(z = 0), \tag{3}$$

where $\Delta T(z = 0)$ is the transmittance change observed for the sample in the focus position. The above relations are only valid in the thin-sample regime, i.e., if L is smaller than the Rayleigh range. To obtain the nonlinear refractive index for thick samples, more complex equations have to be used, as can be seen in [25].

The z-scan setup is equipped with a light source capable of delivering a sufficient peak power for nonlinear experiments, even for materials with small higher-order susceptibilities. Near-infrared pulses with a central wavelength of 797 nm and a pulse energy of 2.5 mJ are generated by a regenerative amplifier (Solstice, Spectra Physics) at a
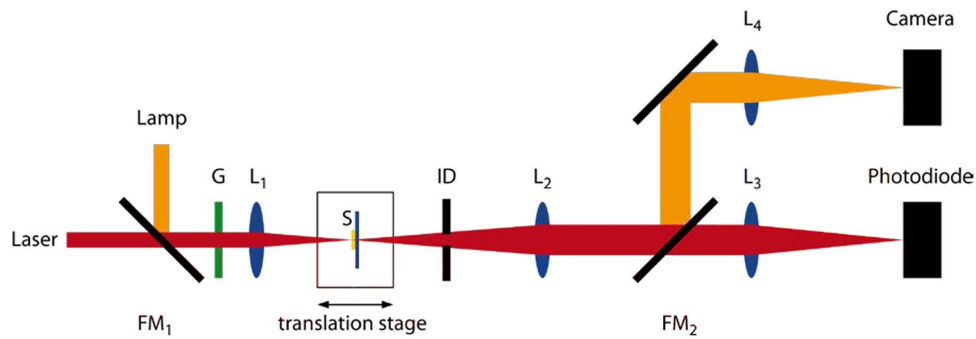
Fig. 1 Sketch of the experimental setup for z-scan measurements. For positioning, the sample plane is mapped onto the camera along the *orange* beam path under illumination with the lamp through lenses $L_{1,2,4}$. The ground glass plate *G* diffuses the *white* light to enable a uniform illumination of the sample *S*. With *G* and the two flip mirrors $FM_{1,2}$ removed, the transmitted light from the laser is focused onto the photodiode along the *red* path and the translation stage is

scanned. The imaginary part of the nonlinear refractive index n_2'' of the sample material is deduced from a z-scan without the use of the iris diaphragm ID, termed open-aperture scan. Clipping of the beam by partial closure of ID is the basis for a closed-aperture scan. In general, both scans are needed to determine the real part of the nonlinear refractive index n_2'

repetition rate of 1 kHz. The pulses pass a grating compressor, which reduces the pulse length to a typical value of 130 fs at the sample position which was confirmed by frequency-resolved optical gating (FROG) [26] measurements. If needed, power attenuation is achieved by neutral density filters. Power fine-tuning is possible with the help of a half-wave plate in combination with a subsequent linear polarizer which also ensures a defined linear polarization state.

The z-scan setup is sketched in Fig. 1, where the laser beam path is depicted by the red line. The p-polarized laser pulses are focused by an achromatic lens L_1 ($f_1 = 25$ mm) onto the sample *S*. The beam waist of $w_0 = 5.9$ μm and the Rayleigh range of $z_R = 84$ μm were characterized by knife-edge scans. The sample is positioned within the *xy* plane perpendicular to the beam propagation direction by manual translation stages. The sample positioning in *z* direction and the actual scan is done by a motorized linear translation stage. The light transmitted through the sample is spatially confined by an optional iris diaphragm in the case of a closed-aperture z-scan. Afterward, the beam is recollimated by the achromatic lens L_2 ($f_2 = 75$ mm) and focused onto a Si photodiode by the lens L_3. The photodiode is read out at 125 MSamples/s, which allows integrating over about 0.2 μs for each laser shot, significantly enhancing the signal-to-background ratio when compared to continuous recording.

For samples with a large surface area compared to the beam waist, no further positioning is necessary. If the specimen covers only a small area in the sample plane, like the gold flakes measured in this work, precise sample positioning is indispensable. For that purpose, a different beam path (confer orange beam path in Fig. 1) is used by inserting two flip mirrors FM_1 and FM_2. White light from
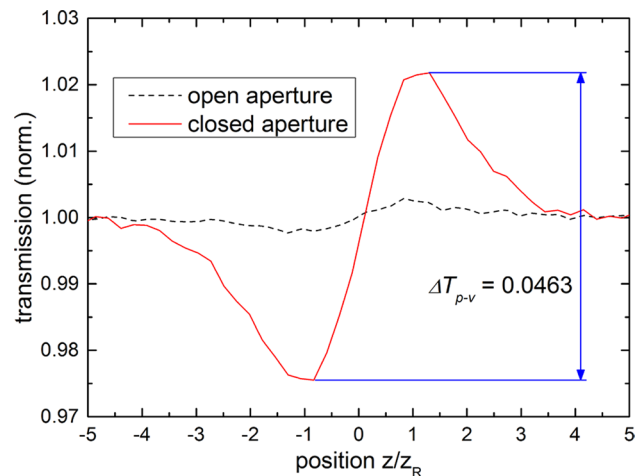
Fig. 2 Z-scan of a fused silica plate of 170 μm thickness. The open-aperture scan (*black dashed line*) shows slight modulation because the outer edges of the spatial beam profile are cut off in the detection path. The real part of the nonlinear refraction index n_2' can be extracted from the transmission change in the closed-aperture scan (*red solid line*). The latter was measured with partially closed iris diaphragm ID

a halogen lamp is diffused by the additional insertion of a ground glass plate *G* (1500 grit) before reaching the sample plane. Hence, the sample plane is evenly illuminated and can be mapped onto a two-dimensional CCD chip (Philips, SPC900NC). In that case, the transmitted light is again collimated by lens L_2, while FM_2 redirects the beam through lens L_4 to the camera.

To demonstrate the functionality of the z-scan setup, a fused silica plate of 170 μm thickness was measured. The normalized z-scan curves were averaged over 20 scans, both for open-aperture and closed-aperture scans, and are

presented in Fig. 2. The scan direction was always from negative to positive z values, i.e., the distance between L_1 and S was increased during a scan. Both curves were measured with a pulse energy of $E = 28.4$ nJ, corresponding to a peak intensity of 0.20 TW/cm^2. The closed-aperture z-scan (red solid curve in Fig. 2) shows the characteristic behavior caused by a refractive index modulation. The overall transmission change is evaluated to be $\Delta T_{p-v} = 0.0463$. According to the modified calculation for thick samples [25], this corresponds to a real part of the nonlinear refractive index of $n_2' = 2.9 \times 10^{-20}$ m^2/W. For fused silica, values between 2 and 5×10^{-20} m^2/W have been reported for near-infrared pulsed laser sources [27–30], proving the reliability of the setup.

An equally shaped but significantly less modulated curve has been measured in the case of the open-aperture z-scan (black dashed curve in Fig. 2). Since the aperture after the sample is removed, we would not expect an antisymmetric characteristic relative to the origin of the z axis. We attribute this residual transmission modulation to a slight clipping of the spatial beam profile at lens L_2, which also acts as an aperture. In both measurements of the fused silica plate (Fig. 2), the transmission change shows a symmetrical modulation for a variation of the focus position, indicating the absence of significant nonlinear absorption resulting in a negligible value of n_2''. This means, we can calculate the purely real value of n_2 directly from the transmission modulation ΔT_{p-v} in the closed-aperture z-scan without initial division by the open-aperture z-scan data. Since the closed-aperture z-scan is not affected by the finite size of L_2, no corrections have to be taken into account.

3 Z-scan measurements of thin single-crystalline gold films

We now apply the z-scan method to a single-crystalline gold flake [31, 32]. Two criteria have to be met by the sample in order to make such measurements possible. On the one hand, its transmittance has to be high enough. On the other hand, the sample must be homogeneous over an area corresponding to the beam size at positions a few times the Rayleigh range away from the focus. Otherwise, the nonlinear transmission changes would be superimposed by aberrations from the sample inhomogeneity.

The gold films we measured had sufficient surface areas of about 100×100 μm^2 with a thickness in the range from 20 to 100 nm, which was determined by transmission measurements at low powers. An increased heat dissipation for thicker gold layers leads to a higher damage threshold [33], at the cost of lower transmission. However, in terms of nonlinearity, thicker flakes have no advantage. Using the absorption coefficient $\alpha = 0.0770$ nm^{-1} from Johnson and

Christy data [34] at the laser central wavelength of 797 nm, the gold flake with a thickness of 63 nm investigated in the following has an effective length of $L_{\text{eff,63 nm}} = 12.89$ nm according to (2), which is already close to the effective length $L_{\text{eff},\infty} = 12.99$ nm in the limit of infinitely thick layers.

The gold flake was prepared on a fused silica glass (thickness 170 μm, same as above). Since the light is attenuated by the gold layer before entering the glass, no nonlinear contributions from the glass are expected for the utilized pulse energy of $E = 32$ nJ. An open-aperture z-scan showed linear behavior, i.e., no variation of transmission beyond the noise floor. From the obtained standard deviation of 1.04 % in this measurement an upper bound for the absolute value of n_2'' of single-crystalline gold can be deduced via (3), giving $|n_2''(\text{Au})| < 0.6 \times 10^{-16}$ m^2/W for $\Delta T(z = 0) = 1.04 \times 10^{-2}$.

The results of 30 consecutive closed-aperture z-scans are shown in Fig. 3a. As one can see, no change in transmission for the first five scans is visible. Afterward, a z-position-dependent transmission modulation arises and increases with each scan. The shape of the selected curves from the scans 10, 20, and 30 in Fig. 3b could be interpreted as an antisymmetric modulation originating from a nonlinear refractive index, superimposed with an increase in transmission due to saturable absorption. The latter has been reported for thin coarse gold films [18]. However, this cannot explain the increasing modulation from scan to scan.

The scanning electron microscopy (SEM) image taken at the middle of the flake after the z-scan measurements (Fig. 3b, inset) reveals the damage of the gold layer with a diameter of about 4 μm. The missing gold film is the reason for the transmission increase in the z-scans, whereas the glass, now exposed to high peak powers, could cause the antisymmetric (with respect to $z = 0$) nonlinear signal contribution. Diffraction at the gold film edge might also contribute to this modulation.

From the conducted z-scans, we conclude that the damage threshold of the single-crystalline gold layer (63 nm thickness) is at the used peak intensity of 0.22 TW/cm^2, corresponding to a pulse energy per area of 0.029 J/cm^2. Since no deviations from the constant gold transmission could be detected within the measurement error (standard deviation for the closed-aperture z-scans of 0.97 %) during the first five closed-aperture z-scans, we obtain an upper bound for the absolute value of n_2' of single-crystalline gold, $|n_2'(\text{Au})| < 1.2 \times 10^{-16}$ m^2/W. In this case of a thin layer, (1) is valid. $\Delta T_{p-v} = 9.7 \times 10^{-3}$ and $L_{\text{eff}} = 12.89$ nm were used for the calculation.

For flat surfaces of gold, as in the demonstrated case, the interaction of the electromagnetic waves with the metal is hindered by the rather small penetration depth. The low effective length L_{eff} [see (2)] of <13 nm is an implication of
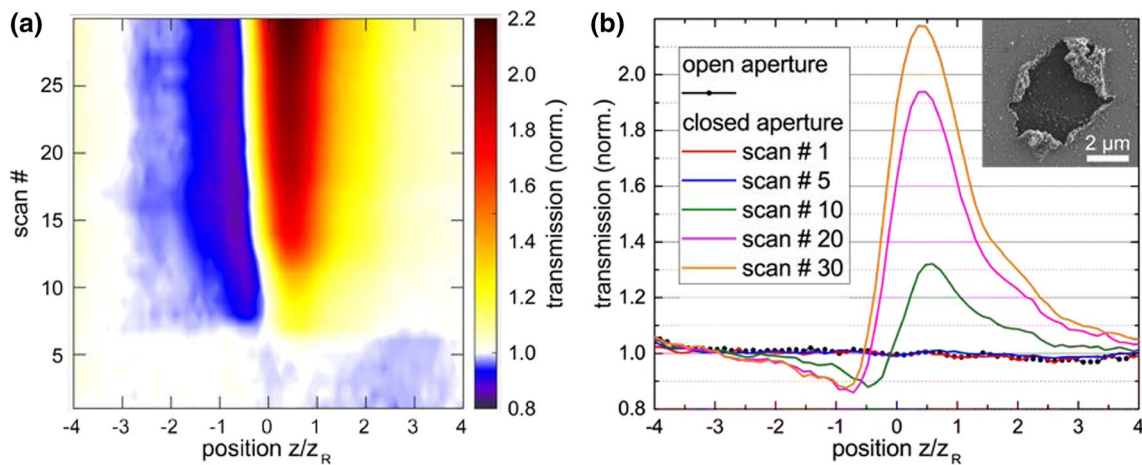
Fig. 3 Z-scan measurements on a single-crystalline gold layer of 63 nm thickness. **a** Transmission maps from 30 consecutively, identical closed-aperture z-scans. **b** The open-aperture z-scan (*black line with dots*) shows no z-dependent variation exceeding the measurements' standard deviation. From this, an upper bound for the absolute value of the imaginary part of the nonlinear refractive index $|n_2''|$ is calculated. The *solid lines* show five selected closed-aperture scans from (**a**). The *curves* for scan nos. 1 and 5 show no variations, the remaining *curves* show systematic z-position-dependent variation increasing from scan to scan. The variation is attributed to laser-induced damage of the gold layer, confirmed by SEM measurements (figure *inset*). Nevertheless, from the first two curves (scan nos. 1 and 5), an upper bound for the absolute value of the real part of the nonlinear refractive index $|n_2'|$ is calculated

the waves being expelled from the gold so that the major contribution to the nonlinear effect arises from the sample's surface region [35]. There are several processes that can contribute to the nonlinearity, e.g., the intraband contribution and the hot-electron contribution, which is described in detail in [17]. The contributions of relevance are determined (and therefore fixed) by their response time in comparison with the laser pulse length and the spectral regime used in the experiment. A way to further enhance the interaction is to use nanostructures. Due to confined and thereby resonantly enhanced optical near-fields that occur at such structures, an increased interaction with the metal can be achieved. For this reason, we introduce a nanostructure that acts as a sensitive probe for nonlinear phase changes in plasmon excitations.

## 4 Intrinsic differential plasmon interferometry

Recent progress in the quantitative selective excitation of multiple eigenmodes [36] in plasmonic nanocircuits based on optical antennas [37, 38] and two-wire transmission lines [39, 40] have paved the way for the experimental demonstration of controlled plasmon propagation based on interference of well-defined modes in more complex nanocircuits [8]. This interference can be utilized to detect changes of the spectral phase difference between the modes.

If one considers the propagation phase of a near-field mode that is subject to small changes when excited at different intensities, such changes can be monitored by

sophisticated near-field probe methods (e.g., NSOM [41] and PEEM [42]) or spectral interferometry [43–45]. The latter reconstructs the complete plasmon propagation phase, but the extraction of small excitation intensity-induced changes remains challenging.

We therefore propose the use of a phase-sensitive plasmonic nanointerferometer that intrinsically translates differences of the propagation phase into a far-field intensity variation which can directly be measured by conventional optical imaging techniques. The outline of such a structure is shown in Fig. 4a. The nanointerferometer is based on two-wire transmission lines supporting a symmetric eigenmode (Fig. 4a, b inset, top) and an antisymmetric eigenmode (Fig. 4a, b inset, bottom). A linear combination of these near-field modes can be excited at the input antenna, resulting in a beating pattern along the propagation direction due to different effective wavelengths of the eigenmodes ($\lambda_{eff}^{sym} = 483$ nm and $\lambda_{eff}^{antisym} = 439$ nm for 780-nm vacuum wavelength). After propagation along the nanostructure, the light is coupled back to the far-field at the two output ports, labeled A and B.

The nanointerferometer was designed using finite-difference time-domain (FDTD) simulations (Lumerical Solutions Inc., FDTD Solutions) to direct a superposition of both modes preferentially to one of the output ports with variable contrast ratios. A simulated far-field image is shown in Fig. 4a, showing a structure where the required mode superposition is generated using a $+45°$ linearly polarized Gaussian beam (NA = 1.4) positioned at the center of an input antenna with overall length of 425 nm.
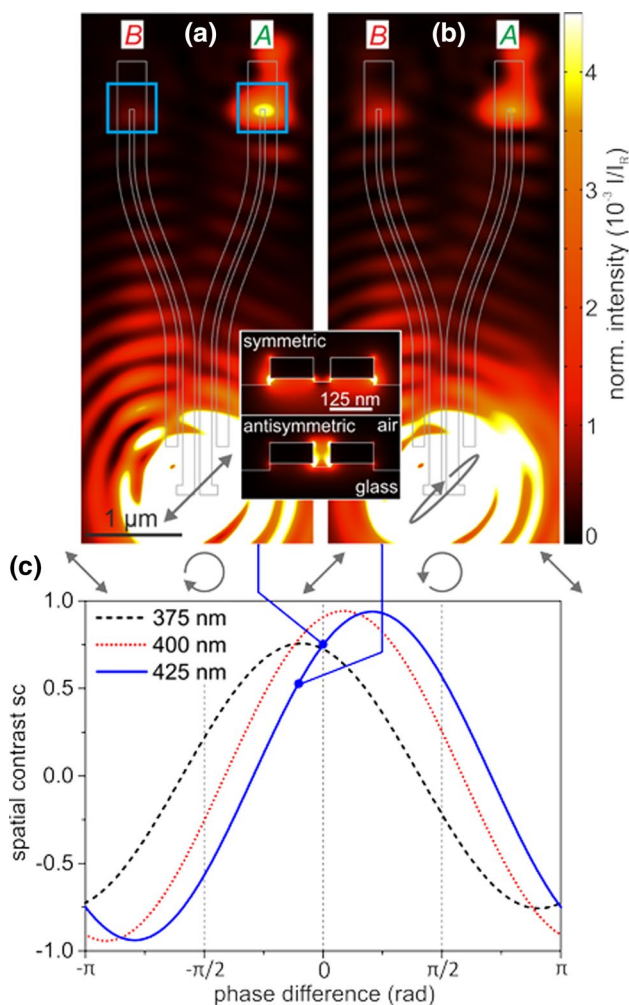
Fig. 4 Principle functionality of interferometry in a plasmonic nanostructure. **a** Simulated far-field image of the phase-sensitive plasmonic nanointerferometer excited at the input antenna (over-all length 425 nm) with a focused Gaussian beam polarized at 45° with respect to the antenna axis, as indicated by the *gray arrow*. The intensity scale is normalized to an unstructured gold surface reflection (I_R). The structure's outline is superimposed as a guide to the eye. The *blue squares* indicate the regions used to evaluate the spatial contrast. **b** Simulated far-field image of the identical structure assuming a change by $-\pi/10$ rad in phase difference between the two eigenmodes, i.e., increasing the ellipticity of the excitation polarization. (*Inset*) Simulated transverse modal profiles of symmetric (*top*) and antisymmetric (*bottom*) eigenmodes for the two-wire transmission line geometry, obtained using a mode solver (Lumerical Solutions Inc., MODE Solutions). **c** Spatial contrast as a function of the introduced change in phase difference between the two eigenmodes for input antenna lengths of 375 (*black dashed line*), 400 (*red dotted line*), and 425 nm (*blue solid line*). The corresponding effective excitation polarization is depicted above

This leads to a predominant routing of the intensity to the right branch and emission from output port *A*.

A quantification of the branching ratio in the nanostructure is achieved by introducing the spatial contrast sc, which is defined as follows

$$\text{sc} = \frac{E(A) - E(B)}{E(A) + E(B)}, \tag{4}$$

where $E(A)$ and $E(B)$ are the energies emitted from the output ports *A* and *B*, respectively, as determined by integrating $0.5 \times 0.5 \ \mu m^2$ regions indicated with blue squares in Fig. 4a. In the linear operation regime, a well-defined polarization of the incoming light results in a certain spatial contrast defined by the relative phase and amplitude of the two excited modes and the exact geometry of the branching region. Spatial contrast values of sc = 0.79 and sc = −0.88 were experimentally obtained in these nanostructures by linearly polarized excitation at +45° and −45° relative to the long wire axis, respectively.

A nonlinear refractive index leads to a phase variation of the propagating plasmons. We expect the process to occur in the antenna region where the local field is largest. If the nonlinear effect varies in magnitude between the two superimposed plasmon modes, e.g., because of different field localization and enhancement, a relative phase change is introduced. Due to the decaying intensities of the propagating modes, phase changes upon propagation caused by nonlinear effects likely only play a minor role.

The potential benefit of this kind of structure for studies of nonlinear effects is due to the phase sensitivity of the spatial contrast sc between the output ports, as can be seen in the reduced spatial contrast in Fig. 4b obtained for a relative phase change of $-\pi/10$ rad.

In the simulation shown in Fig. 4b, the effect of a nonlinearity has been approximated by introducing a phase difference between horizontally and vertically aligned excitation components, corresponding to an effectively elliptical excitation. In the case considered here of a $-\pi/10$ relative phase change, the spatial contrast, as defined in (4), was decreased from 0.75 to 0.53 for the structure featuring an overall antenna length of 425 nm.

To investigate this further, we consider structures that are nominally identical except for the input antenna length that influences the amplitude of each excited mode [36]. Consequently, the structures show varying spatial contrasts for the same +45° linearly polarized excitation in our simulations. The respective results for input antenna lengths of 375, 400, and 425 nm are presented in Fig. 4c. A closer look at the spatial contrast as a function of the introduced relative phase change between the two eigenmodes reveals that the structure with overall antenna length of 400 nm shows the highest spatial contrast for +45° polarized excitation, whereas the other structures have slightly detuned antenna lengths leading to a reduced spatial contrast. Using +45° linear polarized excitation, the spatial contrast of the interferometer with 425 nm antenna length is expected to have the highest sensitivity for relative phase changes. In the following, the behavior

of these structures for varying excitation intensity is investigated experimentally.

The experimental setup used for these studies consists of a Ti: Sapphire oscillator with subsequent LCD-based pulse shaper and high-NA microscope [45, 46]. The oscillator emits laser pulses with a spectrum from 650 to 950 nm (foot width) [46] at a repetition rate of 80 MHz. In combination with a pair of chirped mirrors, the dispersion from transmissive optics is pre-compensated in the pulse shaper. By using the phase-resolved interferometric spectral modulation (PRISM) algorithm [47], a pulse length of below 10 fs is reached at the sample position, measured by second-order autocorrelation. The beam waist of the immersion oil objective (NA = 1.4) has been characterized [46] to be about 260 nm (beam waist for $I = I_{max}/e^2$).

For power-dependent scans, we use a broadband half-wave plate in combination with a linear polarizer. The angle of the wave plate and thereby the power transmitted through the subsequent polarizer is varied in a precise and reproducible way by a motorized rotation stage.

The excitation position of the sample is selected by mounting it on a piezo scanner. The emission position is set independently using a piezo tip–tilt mirror in combination with confocal detection. Spatial maps are scanned and detected in reflection through the same objective by avalanche photodiodes. Instead of confocal detection, a two-dimensional image of the sample plane can be mapped onto a two-dimensional CCD chip (Princeton Instruments, Acton Pixis2kB) [45].

5 Intensity-dependent relative phase change in nanointerferometers

For the experiments, the linear excitation polarization is kept fixed at +45°, resulting in an emission mainly from output *A* (Fig. 4a). As described above, the spatial contrast is modulated if the relative phase between the two excited near-field modes varies. Such a variation would be expected to result from a nonuniform nonlinear refractive index. We test for such a phase change to occur by varying the power of the incident light.

Two identical series of nanointerferometers, S_1 and S_2, were fabricated by focused ion-beam milling (FEI company, Helios NanoLab) from a single-crystalline gold flake deposited on a cover glass [31]. Within each series, the overall input antenna length is increased from structure to structure, resulting in slightly different relative amplitudes of the excited near-field modes. Apart from that, the geometry of the structures is identical.

We selected four of these nanostructures, three of them from series S_1 and one from series S_2. The former are shown in the SEM picture in Fig. 5a. The antenna lengths

for these structures are 375 nm for structure S_1 s (small), 400 nm for structure S_1 m (medium), and 425 nm for the identical structures S_1 l and S_2 l (large).

Figure 6 shows the spatial contrast between the output ports in power-dependent experiments for structures with different antenna lengths (425 nm in Fig. 6a, 400 nm in Fig. 6b, and 375 nm in Fig. 6c). Subsequent series of measurements M_i on the same structure are labeled by the index i in chronological order. The error bars show the standard deviation of all measurements taken at the same power in a single series of measurements. Within each series of measurements, multiple up-and-down scans of the excitation power (called loops from now on) were performed. The intensity scan in a single loop is sketched in the inset of Fig. 6c. Each loop consists of a scan with increasing intensity (labeled *U*) followed by a scan with decreasing intensity (labeled *D*). A series of measurements was stopped when the average spatial contrast within *U* differed by more than 10 % from the average spatial contrast within *D* in a single loop. Those irregularities can be an indicator for sample drift, because the spatial contrast is dependent on the exact in-coupling position [36]. Since the contrast changes occurred mainly after a few loops close to the antenna damage threshold, we attribute it to sample degradation after an initial antenna deformation at the highest power within a loop.

SEM pictures of the three structures of series S_1 taken after the intensity-dependent scans are shown in Fig. 5b. The antennas have suffered visible damage and are deformed, which can be seen more clearly in the inset showing the 425 nm antenna of structure S_1 l. All three antennas were damaged at some point during the measurements, regardless if the highest used peak intensity was 52 or 127 GW/cm^2. Therefore, we determine the damage threshold of the investigated phase-sensitive plasmonic nanointerferometers to an upper bound of 52 GW/cm^2, corresponding to a threshold intensity a factor of 0.23 relative to the threshold for homogenous gold layers determined above from the *z*-scan measurements. In terms of pulse energy per area, damage occurs at 0.48 J/cm^2. However, the observation that the gold film can withstand a given peak power for multiple seconds before taking visible damage was also made in the *z*-scan measurements in Sect. 3.

The fact that the spatial contrast remained constant during a series of measurements until a rapid change at a certain point gives a hint that, until then, the nanointerferometers also withstood the incident laser pulses without taking damage. When a series of measurements was repeated afterward on the same wire, the spatial contrast again was constant for multiple loops. Nevertheless, the tendency that the absolute value of the spatial contrast gets smaller for repeated series of measurements on the same structure can be seen for all three antenna lengths. This tendency was

Fig. 5 SEM pictures of nanointerferometers before and after power-dependent excitation scans. **a** SEM picture of the three used structures of series S_1 right after fabrication. Antennas with the lengths 375, 400, and 425 nm (*left to right*) show no sign of damage. **b** SEM picture of the same structures after the power-dependent scans. All three antennas have clearly taken damage. The *inset* shows the partly melted 425 nm antenna of structure S_1 l
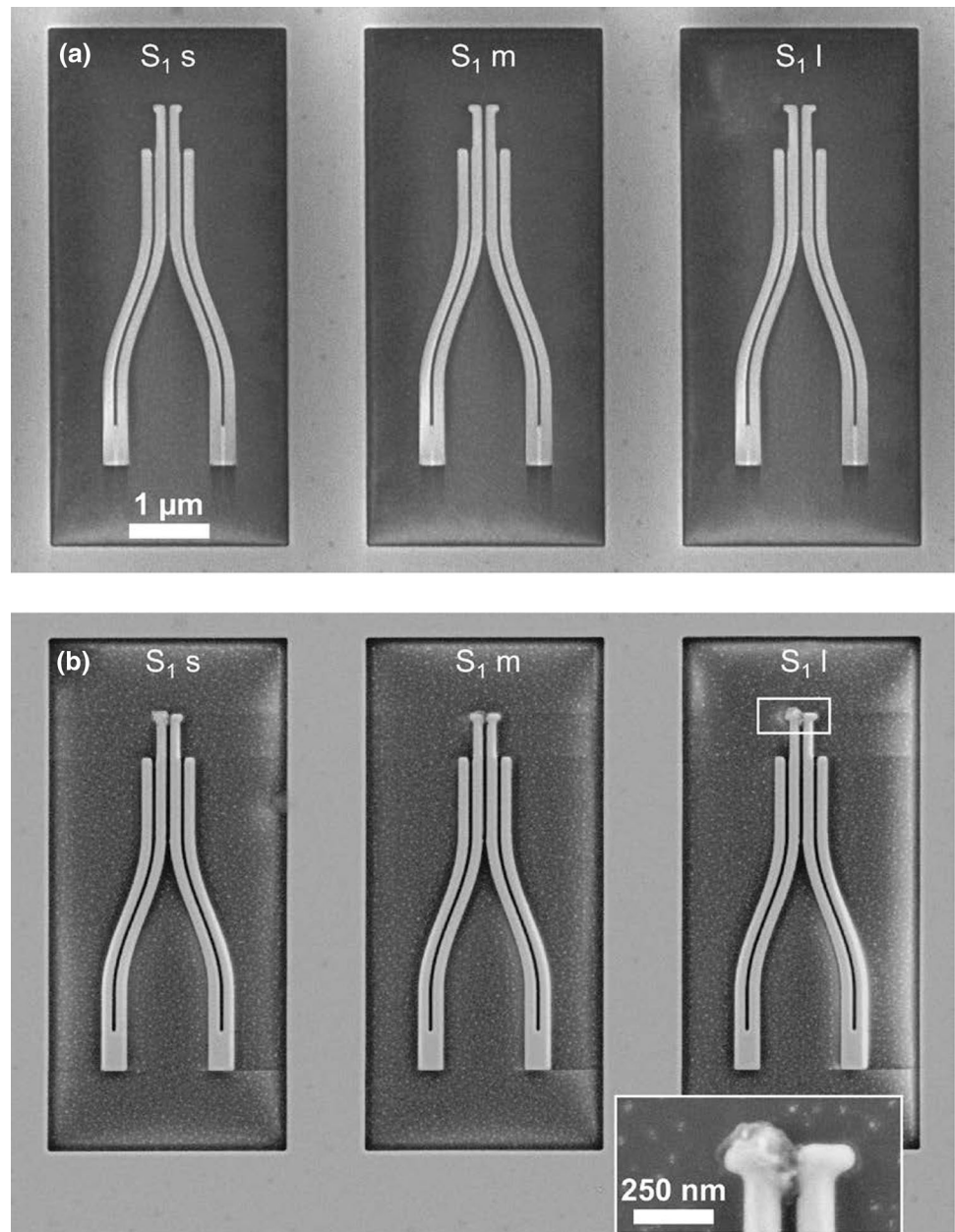

also observed in simulations, where parts of one antenna arm were removed to mimic the damage. Within one series of measurements, the power-dependent deviation of the spatial contrast is in the range of the error bars, i.e., no nonlinear effect is observable. Typical errors are in the order of 5 % of the spatial contrast value. To achieve experimentally detectable spatial contrast variations exceeding the measurement uncertainties using our most sensitive structures (S_1 l and S_2 l with an overall antenna length of 425 nm), according to the simulation model (Fig. 4c) a phase difference between the two eigenmodes of 0.07 rad or more would be required. Thus, we conclude that the experimentally achieved nonlinear relative phase change between the

symmetric and the antisymmetric plasmonic eigenmode is below 0.07 rad.

6 Conclusions

We have investigated the nonlinear refractive index and the damage threshold of gold in thin films and plasmonic nanostructures. The z-scan method was implemented and verified on a fused silica film of 170 μm thickness. The obtained nonlinear refractive index, $n_2(SiO_2) = 2.9 \times 10^{-20}$ m²/W, is in accordance with other reported values of z-scan measurements with near-infrared pulsed laser sources.
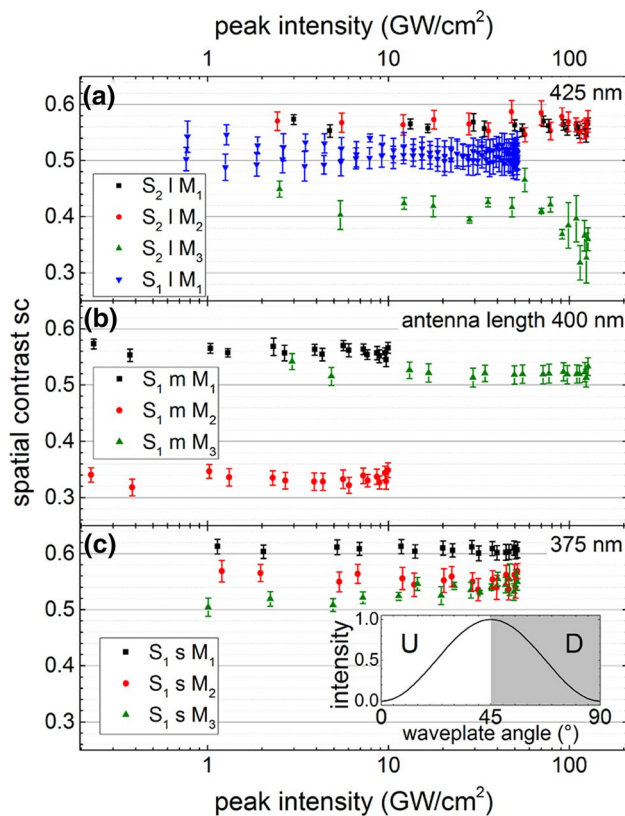
Fig. 6 Power-dependent scans of the spatial contrast in nanointerferometers. *Each color* shows a power-dependent series of measurements M_i on nanointerferometers with overall antenna lengths of **a** 425 nm, **b** 400 nm, and **c** 375 nm. Each series M_i consists of multiple up-and-down scans (loops) in excitation power. A single loop is depicted in the *inset* in (**c**). The average spatial contrast change between a pair of consecutive scans upwards (*U*) and downward (*D*) is used as an indicator for sample drifts or laser-induced damage. The constant spatial contrast within each series of measurements is used to set an upper bound for the relative phase change of $\Delta\varphi < 0.07$ rad between the two excited plasmonic eigenmodes

Z-scan measurements of thin gold layers yielded a damage threshold of 0.22 TW/cm^2 and upper bounds of the real and imaginary parts of the nonlinear refractive index of $|n_2'(\mathrm{Au})| < 1.2 \times 10^{-16}$ m^2/W and $|n_2''(\mathrm{Au})| < 0.6 \times 10^{-16}$ m^2/W, respectively, for a single-crystalline gold film with a thickness of 63 nm.

A nanointerferometer was proposed as a sensitive probe for the relative phase change between two plasmonic eigenmodes of the nanostructures, leading to a change in spatial contrast between its two output ports. Nanointerferometers with different input antenna lengths and thereby different spatial contrasts of the emission signals in the linear regime have been investigated experimentally. The interferometers showed damage thresholds with a factor of 0.23 relative to homogeneous gold films. Furthermore, an upper bound for the introduced relative phase change of $\Delta\varphi < 0.07$ rad

between the plasmonic modes was determined in the power-dependent measurements.

The sensitivity of the demonstrated methods could further be enhanced by the use of shorter laser pulses and fine-tuning the design of the plasmonic nanointerferometers. With these improvements on *z*-scan and interferometric methods on single-crystalline gold, the determination of the nonlinear refractive index is in reach.

References

1. S.A. Maier, *Plasmonics: Fundamentals and Applications* (Springer, Berlin, 2007)
2. W.L. Barnes, A. Dereux, T.W. Ebbesen, Nature **424**, 824 (2003)
3. M. Stockman, Opt. Express **19**, 22029 (2011)
4. L. Novotny, N. van Hulst, Nat. Photonics **5**, 83 (2011)
5. P. Biagioni, J.-S. Huang, B. Hecht, Rep. Prog. Phys. **75**, 024402 (2012)
6. Y. Fang, Z. Li, Y. Huang, S. Zhang, P. Nordlander, N.J. Halas, H. Xu, Nano Lett. **10**, 1950 (2010)
7. H. Wei, Z. Wang, X. Tian, M. Käll, H. Xu, Nat. Commun. **2**, 387 (2011)
8. C. Rewitz, G. Razinskas, P. Geisler, E. Krauss, S. Goetz, M. Pawłowska, B. Hecht, T. Brixner, Phys. Rev. Appl. **1**, 014007 (2014)
9. G. Lenz, J. Zimmermann, T. Katsufuji, M.E. Lines, H.Y. Hwang, S. Spälter, R.E. Slusher, S.-W. Cheong, J.S. Sanghera, I.D. Aggarwal, Opt. Lett. **25**, 254 (2000)
10. A. Reiserer, J.-S. Huang, B. Hecht, T. Brixner, Opt. Express **18**, 11810 (2010)
11. P. Ginzburg, A. Hayat, N. Berkovitch, M. Orenstein, Opt. Lett. **35**, 1551 (2010)
12. S. Palomba, L. Novotny, Phys. Rev. Lett. **101**, 056802 (2008)
13. J. Renger, R. Quidant, N. van Hulst, L. Novotny, Phys. Rev. Lett. **104**, 046803 (2010)
14. M. Lippitz, M.A. van Dijk, M. Orrit, Nano Lett. **5**, 799 (2005)
15. T. Hanke, G. Krauss, D. Träutlein, B. Wild, R. Bratschitsch, A. Leitenstorfer, Phys. Rev. Lett. **103**, 257404 (2009)
16. M. Hentschel, T. Utikal, H. Giessen, M. Lippitz, Nano Lett. **12**, 3778 (2012)
17. R.W. Boyd, Z. Shi, I. De Leon, Opt. Commun. **326**, 74 (2014)
18. D.D. Smith, Y. Yoon, R.W. Boyd, J.K. Campbell, L.A. Baker, R.M. Crooks, M. George, J. Appl. Phys. **86**, 6200 (1999)
19. P. Wang, Y. Lu, L. Tang, J. Zhang, H. Ming, J. Xie, F.-H. Ho, H.-H. Chang, H.-Y. Lin, D.-P. Tsai, Opt. Commun. **229**, 425 (2004)
20. N. Rotenberg, A.D. Bristow, M. Pfeiffer, M. Betz, H.M. van Driel, Phys. Rev. B **75**, 155426 (2007)
21. E. Xenogiannopoulou, P. Aloukos, S. Couris, E. Kaminska, A. Piotrowska, E. Dynowska, Opt. Commun. **275**, 217 (2007)
22. M. Sheik-Bahae, A.A. Said, E.W. Van Stryland, Opt. Lett. **14**, 955 (1989)
23. M. Sheik-Bahae, A. Said, T.-H. Wei, D.J. Hagan, E.W. Van Stryland, IEEE J. Quantum Electron. **26**, 760 (1990)
24. R. Sutherland, *Handbook of Nonlinear Optics*, 2nd edn. (CRC Press, London, 2003)
25. P.B. Chapple, J. Staromlynska, R.G. McDuff, JOSA B **11**, 975 (1994)

26. R. Trebino, K.W. DeLong, D.N. Fittinghoff, J.N. Sweetser, M.A. Krumbügel, B.A. Richman, D.J. Kane, Rev. Sci. Instrum. **68**, 3277 (1997)
27. D. Milam, Appl. Opt. **37**, 546 (1998)
28. H.I. Elim, W. Ji, F. Zhu, Appl. Phys. B **82**, 439 (2006)
29. R. DeSalvo, A.A. Said, D.J. Hagan, E.W. van Stryland, M. Sheik-Bahae, IEEE J. Quantum Electron. **32**, 1324 (1996)
30. T. Olivier, F. Billard, H. Akhouayri, Opt. Express **12**, 1377 (2004)
31. J.-S. Huang, V. Callegari, P. Geisler, C. Brüning, J. Kern, J.C. Prangsma, X. Wu, T. Feichtner, J. Ziegler, P. Weinmann, M. Kamp, A. Forchel, P. Biagioni, U. Sennhauser, B. Hecht, Nat. Commun. **1**, 150 (2010)
32. X. Wu, R. Kullock, E. Krauss, B. Hecht, Cryst. Res. Technol. **50**, 595 (2015)
33. C. Kern, M. Zürch, J. Petschulat, T. Pertsch, B. Kley, T. Käsebier, U. Hübner, C. Spielmann, Appl. Phys. A **104**, 15 (2011)
34. P.B. Johnson, R.W. Christy, Phys. Rev. B **6**, 4370 (1972)
35. R. de Nalda, R. del Coso, J. Requejo-Isidro, J. Olivares, A. Suarez-Garcia, J. Solis, C.N. Afonso, JOSA B **19**, 289 (2002)
36. P. Geisler, G. Razinskas, E. Krauss, X.-F. Wu, C. Rewitz, P. Tuchscherer, S. Goetz, C.-B. Huang, T. Brixner, B. Hecht, Phys. Rev. Lett. **111**, 183901 (2013)
37. P. Mühlschlegel, H.-J. Eisler, O.J.F. Martin, B. Hecht, D.W. Pohl, Science **308**, 1607 (2005)
38. J.-S. Huang, T. Feichtner, P. Biagioni, B. Hecht, Nano Lett. **9**, 1897 (2009)
39. M. Schnell, P. Alonso-González, L. Arzubiaga, F. Casanova, L.E. Hueso, A. Chuvilin, R. Hillenbrand, Nat. Photonics **5**, 283 (2011)
40. P.M. Krenz, R.L. Olmon, B.A. Lail, M.B. Raschke, G.D. Boreman, Opt. Express **18**, 21678 (2010)
41. E. Verhagen, M. Spasenović, A. Polman, L. (Kobus) Kuipers, Phys. Rev. Lett. **102**, 203904 (2009)
42. M. Cinchetti, A. Gloskovskii, S.A. Nepjiko, G. Schönhense, H. Rochholz, M. Kreiter, Phys. Rev. Lett. **95**, 047601 (2005)
43. L. Lepetit, G. Cheriaux, M. Joffre, JOSA B **12**, 2467 (1995)
44. C. Rewitz, T. Keitzl, P. Tuchscherer, J.-S. Huang, P. Geisler, G. Razinskas, B. Hecht, T. Brixner, Nano Lett. **12**, 45 (2012)
45. C. Rewitz, T. Keitzl, P. Tuchscherer, S. Goetz, P. Geisler, G. Razinskas, B. Hecht, T. Brixner, Opt. Express **20**, 14632 (2012)
46. M. Pawłowska, S. Goetz, C. Dreher, M. Wurdack, E. Krauss, G. Razinskas, P. Geisler, B. Hecht, T. Brixner, Opt. Express **22**, 31496 (2014)
47. T. Wu, J. Tang, B. Hajj, M. Cui, Opt. Express **19**, 12961 (2011)